

# Insights into Past Ocean Proxies from Micron-scale Mapping of Sulfur Species in Carbonates

Catherine V. Rose<sup>1,2\*</sup>, Samuel M. Webb<sup>3</sup>, Matthew Newville<sup>4</sup>, Antonio Lanzirotti<sup>4</sup>, Jocelyn A. Richardson<sup>2</sup>, Nicholas J. Tosca<sup>5</sup>, Jeffrey G. Catalano<sup>2</sup>, Alexander S. Bradley<sup>2</sup>, David A. Fike<sup>2</sup>

<sup>1</sup>*School of Earth & Environmental Sciences, University of St Andrews, Fife, KY16 9AL, UK;*

<sup>2</sup>*Dept. of Earth and Planetary Sciences, Washington University in St Louis, 1 Brookings Drive, St Louis, MO 63130, USA;*

<sup>3</sup>*Stanford Synchrotron Radiation Lightsource, Stanford University, Menlo Park, CA 94025, USA;*

<sup>4</sup>*Consortium for Advanced Radiation Sources, University of Chicago, Chicago, IL 60637, USA;*

<sup>5</sup>*Department of Earth Sciences, University of Oxford, Oxford, OX1 3AN, UK.*

\*Corresponding author: [cvr@st-andrews.ac.uk](mailto:cvr@st-andrews.ac.uk)

## ABSTRACT

Geological reconstructions of global ocean chemistry and atmospheric oxygen concentrations over Earth history frequently rely on the abundance and stable isotopic composition ( $\delta^{34}\text{S}$ ) of sulfur-bearing compounds. Carbonate-associated sulfate (CAS), sulfate bound within a calcium carbonate mineral matrix, is among the most commonly interrogated sulfur mineral phases. However, recent work has revealed variability in  $\delta^{34}\text{S}_{\text{CAS}}$  values that cannot be explained by evolution of the marine sulfate reservoir, challenging the common interpretation that CAS is inherently a high-fidelity record of seawater sulfate. To investigate the source of this inconsistency, we used X-ray spectromicroscopy to map the  $\mu\text{m}$ -scale distribution of S-bearing sedimentary phases in Ordovician-aged ( $\sim 444$  Ma) shallow marine carbonates from Anticosti

26 Island, Quebec. Clear differences in the abundance of CAS are observed between cements and  
27 fossils, suggesting that variance in bulk-rock data could be a consequence of component mixing  
28 and that coupled synchrotron-petrographic screening can identify the carbonate components that  
29 are most likely to retain primary CAS. Furthermore, we observe multiple, distinct moieties of  
30 sulfate (both inorganic and organic). Differences in these moieties among fossil clades could  
31 provide new insights into biomineralization mechanisms in extinct organisms.

## INTRODUCTION

Stable isotope ratios of C- and S-bearing phases in sedimentary rocks retain an extensive record of environmental change throughout Earth history (Garrels and Lerman, 1981; Berner, 2006). Carbonate-associated sulfate (CAS), sulfate trapped within a calcium carbonate mineral matrix at typical concentrations of ~100 – 10,000 ppm, is one such phase (Burdett et al., 1989). The stable isotope ratio of sulfur in CAS ( $\delta^{34}\text{S}_{\text{CAS}}$ ) is usually interpreted as a primary record of the stable isotopic composition of sulfate sulfur in contemporaneous seawater sulfate (Fike and Grotzinger, 2008; Gill et al., 2011). However, reports of coeval but discordant  $\delta^{34}\text{S}_{\text{CAS}}$  are common (Fike and Grotzinger, 2008; Ries et al., 2009). Furthermore,  $\delta^{34}\text{S}_{\text{CAS}}$  data from individual locations show more variability than could plausibly be attributed to a primary marine signal (Jones and Fike, 2013; Fike et al., 2015). Higher-resolution analyses of individual carbonate components (e.g., micrite, spar) and fossils (e.g., brachiopods, bryozoa, crinoids) reveal even larger degrees of isotopic variability in CAS at smaller spatial scales (Present et al., 2015). This variability challenges our assumption that bulk-carbonate CAS uniformly derives from seawater.

To assess the role of compositional heterogeneity in driving the observed variability in  $\delta^{34}\text{S}_{\text{CAS}}$ , it is critical to understand how sulfate and sulfide phases are associated with diverse carbonate components. Carbonate petrography can reveal the mixture of fossil fragments, micrite, and various cements that comprise the rock, along with detrital siliciclastic material and other authigenic minerals. Furthermore, petrographic textures often can distinguish the nature and relative timing of primary/early diagenetic marine components from later diagenetic cements. Since the amount of these components varies among samples, differences in the abundance of CAS or other S-bearing phases among carbonate components could drive the bulk  $\delta^{34}\text{S}$  variability in the rock record. We used X-ray spectromicroscopy to produce  $\mu\text{m}$ -scale maps of the distribution of sulfur phases in an Ordovician-aged (~444 Ma) oncoid grainstone from

Anticosti Island, Quebec (Jones et al., 2011; see GSA Data Repository; Fig. S1). The sample is from a stratigraphic section that spans the Hirnantian glaciation and mass extinction, and which records scattered bulk-rock  $\delta^{34}\text{S}_{\text{CAS}}$  values (18-32‰; Jones and Fike, 2013). Here we identified and mapped sulfide (e.g. pyrite), inorganic sulfate (canonical ‘CAS’) and novel organosulfate phases, and determined their petrographic association with various carbonate components.

## **SULFUR SPECIATION IN ORDOVICIAN CARBONATES**

Sulfur K-edge X-ray Absorption Near-edge Structure (XANES) measurements produce distinguishable absorbance spectra from the analysis of samples containing sulfate, sulfide, or both (Fig. 1A). These spectra are sensitive to an array of S species if present and uniquely enable the identification of multiple forms of inorganic and organic sulfate; both are present in these Ordovician carbonates (Fig. 1B). This technique generates maps of the distribution and abundance of CAS within complex sedimentary carbonates, leading to a better understanding of how this proxy is incorporated, and subsequently altered, in geologic samples. Furthermore, mapping of the spatial distribution of inorganic and organic phases of sulfate that together comprise CAS, provide new insights into the biomineralization mechanisms of extinct clades of organisms.

The spatial distribution of sulfur species varies across different carbonate components (Fig. 2A-C). Sulfide predominantly occurs as finely disseminated grains of pyrite within micrite, and in variable abundance in skeletal and non-skeletal (e.g., oncoid, intraclast) grains (see GSA Data Repository). Sulfide is absent from equant spar cements. This variability in sulfide content suggests that micrite and grains are differentially sensitive to sulfide oxidation, which is important because sulfide oxidation prior to and during traditional bulk-rock CAS extraction is likely to be a major source of variation in measured  $\delta^{34}\text{S}_{\text{CAS}}$  (Wotte et al., 2012).

Sulfate concentration strongly correlates with carbonate component: micrite, skeletal and non-skeletal grains, and cement have very different CAS concentrations (Fig. 2C). Micrite has a uniform texture but could have had several origins by analogy with Recent lime mud: (i) carbonate mud precipitated from supersaturated seawater; (ii) mud derived from the breakdown of calcareous algae; (iii) detrital carbonate mud; (iv) mucilaginous microbial ooze; or (v) *in situ* recrystallization by endolithic algae. Sulfate concentrations differ among various micritic components in our sample. We defined regions of interest (ROIs) within the sample based on petrographic analysis and used the ROIs to compare concentrations of sulfate among sample components (Figs. 2B and 4). Within each ROI we measured several hundred to several thousand sulfate concentrations, in 5  $\mu\text{m}$  x 5  $\mu\text{m}$  pixels. Pairwise comparisons of the mean sulfate concentrations between ROIs within each sector showed that nearly all could be distinguished ( $p < 0.05$ , adjusted for multiple comparisons; see GSA Data Repository). The mean sulfate concentration and its standard error for several components included micrite adjacent to a recrystallized gastropod shell ( $\sim 64.1 \pm 0.3$  ppm; ROI 5), micritic coatings around remnant skeletal components ( $\sim 39.9 \pm 0.8$  ppm and  $70.1 \pm 2.1$  ppm; ROIs 8 and 9) and non-skeletal fragments ( $\sim 82.0 \pm 0.9$  ppm; ROI 2), and the fine-grained detrital material within the gastropod shell ( $\sim 30.9 \pm 0.3$  ppm and  $68.0 \pm 0.9$  ppm; ROIs 6 and 7; see GSA Data Repository). Quantifying spatial variability within sulfate in these different forms of micrite is critical because it is often targeted in studies of ancient sedimentary rocks as a homogeneous component assumed to passively record ocean biogeochemical signals (Kaufman et al., 1991; Saltzman et al., 1998; Kump et al., 1999). Skeletal and non-skeletal grains also show variable sulfate concentrations ( $190.0 \pm 2.0$  ppm and  $44.4 \pm 0.4$  ppm; ROIs 4 and 1), while the surrounding cement contains variable but extremely low sulfate content (near detection limit; ROI 3). This variability in sulfate concentration is reproduced between grains, micrite and cement across a

thin section. An additional mapped sector in the same thin section records sulfate concentrations for skeletal grains ( $50.8 \pm 1.1$  ppm; ROI 19), non-skeletal grains ( $198.6 \pm 1.2$ ; ROI 16), micritic coatings ( $105.5 \pm 1.1$  ppm; ROI 17), and cement ( $5.2 \pm 0.3$  ppm; ROI 10; Figs. 3A-C and 4).

### **Distinct sulfate moieties**

Detailed examination of the XANES spectra around the sulfate white line<sup>1</sup> in these components reveals three distinct sulfate moieties within a single region (Figs. 2D, 3D). At the highest energy (2482.7 eV), there is an inorganic sulfate phase, such as typically seen in abiotic calcite and which is likely canonical CAS. At a slightly lower energy (2482.5 eV), there is another inorganic sulfate component; the downshift of this phase (hereafter referred to as ‘distorted’) reflects a likely distortion of the carbonate lattice relative to that of calcite, akin to that found in aragonite (Fernández-Díaz et al., 2010) (see GSA Data Repository). At  $\sim 2481.4$  eV, there is a third organosulfate moiety, a sulfate ester requiring active biological synthesis (Tamenori et al., 2014). Each of these three sulfate moieties has a different origin, potentially representing distinct biological and/or biogeochemical processes during deposition, lithification, and subsequent alteration (i.e., diagenesis). Information about these individual components is lost during traditional CAS acid extraction. Standard CAS protocols extract the organosulfate component, which undergoes hydrolysis in acidic conditions – a process that can also give rise to a S isotopic fractionation (Burlingham et al., 2003). Thus, complex micro-scale speciation of sulfate within and between individual samples may also contribute to the unexpectedly large scatter often observed in bulk  $\delta^{34}\text{S}_{\text{CAS}}$  data (Fike et al., 2015).

<sup>1</sup> *White line* is the term attributed to the first sharp rise in a XAS spectrum and corresponds to transitions of electrons to unfilled bound states.

## DISCUSSION

These S speciation maps help constrain the relative timing and geochemical conditions associated with cementation and early diagenetic events (Figs. 2B, 3B). For example, the center of the gastropod in Fig. 2B contains syndepositional detrital material with variable but low sulfate concentrations (micrite  $\sim 30.9 \pm 0.3$  ppm, detrital grain  $\sim 68.0 \pm 0.9$  ppm; ROIs 6 and 7). Adjacent grains with micritized coatings have higher, inorganic sulfate concentrations ( $\sim 82.0 \pm 0.9$  ppm; ROI 2); this is likely associated with calcitization (Fernández-Díaz et al., 2010). The increase in sulfate at the grain rims suggests that micritization and neomorphism occurred in the presence of sulfate-rich fluids (seawater or porewaters in open communication with it), which could reflect increased sulfate uptake in the smaller micrite grains and/or increased substitution of sulfate in the calcite matrix (Fig. 2C). These non-skeletal grains record higher concentrations of organosulfate and a distorted inorganic sulfate moiety caused by different carbonate lattice conditions, similar to aragonite (Figs. 2D, 3D; Fernández-Díaz et al., 2010). However, metastable aragonite reverts to calcite on a  $10^7$  year timescale (the oldest known record of intact aragonite is found in Pennsylvanian mollusks (Balthasar et al., 2011)), so this distorted component is not expected to be within aragonite *per se* but rather a calcite with similar lattice spacing for the incorporation of sulfate (see GSA Data Repository). The originally aragonitic shell of the adjacent gastropod subsequently dissolved and was replaced by later calcite cement with very low sulfate concentrations (near detection limit; Fig. 2B, ROI 3).

Diagenetic effects can be deciphered by careful investigation of variations in major and trace element concentration. For example, Sr and Mn are good indicators for diagenetic alteration: Sr is abundant in seawater and carbonates that precipitate from it, decreasing in abundance with progressive diagenetic recrystallization; Mn is found in only trace quantities in oxic seawater and primary marine carbonates; however, it is abundant in anoxic fluids and its abundance can

increase in carbonates diagenetically altered in the presence of later anoxic fluids. Complementary synchrotron  $\mu$ m-scale trace element analyses can provide information about the environmental histories of individual petrographic components (e.g., Fig. 2E,F). For example, the abundance of Fe and Mn in the cement replacing the gastropod shell indicates the cements formed in association with anoxic fluids in which these metals are soluble (Figs. 2E,F, 3E,F).

The identification of organosulfate components was unexpected and may provide insights into biomineralization mechanisms of extinct clades of organisms. Organosulfate could represent a chemical fossil of calcification potentially mediated by organosulfate-bearing polysaccharides (Cuif et al., 2008; Trong Nguyen et al., 2014). Sulfate concentrations are highest in the cellular framework of a dasyclad alga, which shows contributions from inorganic and organic sulfate (Fig. S2A-E). This fossilized organosulfate is inferred to derive from sulfate-bearing polysaccharides, rather than inorganic lattice-substituted sulfate (Gorzelak et al., 2013). In modern coral skeletons, XRF mapping has shown that sulfate is associated with organic fibers related to the sites of calcification (Cuif et al., 2003). Specifically, banding patterns of sulfate have been imaged in fibrous parts of coral septa, evincing a biochemical zonation that corresponds to the step-by-step growth of fibers. These sulfate bands can be diagnostic among extant coral clades, with more distinct banding recorded in *Montastrea* than in *Lophelia*, and weaker signals observed in *Favia* (Cuif et al., 2003). Our results demonstrate the ability to distinguish inorganic from organic moieties of sulfate in a variety of carbonate grains (Figs. 2, 3) and fossil algae (Fig. S2) and speculate that organosulfate templates were involved in the precipitation of calcitic and aragonitic biocrystals of mollusk shells or coral skeletons.

## SUMMARY

Variation in CAS among various carbonate components - not all of which recording a primary



signal - presents a major challenge to using  $\delta^{34}\text{S}_{\text{CAS}}$  records from bulk carbonates to understand the evolution of Earth's atmosphere and oceans. A basic assumption of the CAS proxy is that it is evenly distributed within sedimentary carbonates, reflecting a homogenous source from the ocean. However, primary CAS reflects the ambient sulfate pool from which the carbonate component precipitated whether it be seawater or porewater. Thus, early marine cements forming in porefluids can have a primary CAS signature that may be reflective of marine conditions, whereas, marine fossils that recrystallized in chemically evolved porefluids may incorporate non-marine CAS. The data presented here show that CAS abundances vary among fossils, muds, and cement components, and that at least three distinct sulfate moieties are preserved (Figs. 2-3, S2), all of which contribute variably to the bulk chemistry of the sample (see GSA Data Repository; Figs. S4-S6). The  $\delta^{34}\text{S}$  of sulfate among the various carbonate components and classes of sulfate moieties cannot be assumed to be identical to each other or to all uniformly record coeval seawater sulfate; given the diversity in their provenance, the  $\delta^{34}\text{S}$  of distinct sulfate components could be quite different (Present et al., 2015). Bulk-rock  $\delta^{34}\text{S}_{\text{CAS}}$  will reflect the weighted mixing of the  $\delta^{34}\text{S}_{\text{CAS}}$  of these carbonate components and moieties of sulfate, each with their own variable composition and diagenetic histories. Stratigraphically varying mixtures of distinct sulfate-bearing components, rather than any change in the marine sulfate reservoir itself, could contribute to the scattered bulk-rock  $\delta^{34}\text{S}_{\text{CAS}}$  data spanning the late-Ordovician Hirnantian glaciation and mass extinction records (Jones and Fike, 2013; Rose et al., 2019).

## ACKNOWLEDGEMENTS

The authors thank George Sevastopulo and the anonymous reviewers for their comments that improved this manuscript. Laboratory work and analyses were supported by a Steve Fossett Fellowship awarded to CVR, a DOE/BER (DE-SC0014613) grant, NSF/EAR (#0951509;

#1229370) grants, an Agouron Institute grant, a Packard Fellowship, and a Hanse-Wissenschaftskolleg Fellowship awarded to DAF, and an NSF Career Grant (EAR-1056480) awarded to JGC. Use of the Stanford Synchrotron Radiation Lightsource, SLAC National Accelerator Laboratory, is supported by the U.S. Department of Energy, Office of Science, Office of Basic Energy Sciences under Contract No. DE-AC02-76SF00515. The contents of this publication are solely the responsibility of the authors and do not necessarily represent the official views of NIGMS or NIH. Analyses were also performed at GeoSoilEnviroCARS (The University of Chicago, Sector 13), Advanced Photon Source (APS), Argonne National Laboratory. GeoSoilEnviroCARS is supported by the National Science Foundation - Earth Sciences (EAR - 1634415) and Department of Energy-GeoSciences (DE-FG02-94ER14466). This research used resources of the Advanced Photon Source, a U.S. Department of Energy (DOE) Office of Science User Facility operated for the DOE Office of Science by Argonne National Laboratory under Contract No. DE-AC02-06CH11357.

## REFERENCES CITED

- Balthasar, U., Cusack, M., Faryma, L., Chung, P., Holmer, L.E., Jin, J., Percival, I.G., and Popov, L.E., 2011, Relic aragonite from Ordovician-Silurian brachiopods: Implications for the evolution of calcification: *Geology*, v. 39, p. 967–970.
- Berner, R.A., 2006, GEOCARBSULF: A combined model for Phanerozoic atmospheric O<sub>2</sub> and CO<sub>2</sub>: *Geochimica et Cosmochimica Acta*, v. 70, p. 5653–5664.
- Burdett, J.W., Arthur, M.A., and Richardson, M., 1989, A Neogene seawater sulfate isotope age curve from calcareous pelagic microfossils.: *Earth and Planetary Science Letters*, v. 94, p. 189–198.
- Burlingham, B.T., Pratt, L.M., Davidson, E.R., Shiner Jr, V.J., Fong, J., and Widlanski, T.S.,

222 2003, S Isotope Effect on Sulfate Ester Hydrolysis: Mechanistic Implications: Journal of the  
223 American Chemical Society, v. 125, p. 13036–13037.

224 Cuif, J.-P., Dauphin, Y., Doucet, J., Salome, M., and Susini, J., 2003, XANES mapping of  
225 organic sulfate in three scleractinian coral skeletons: *Geochimica et Cosmochimica Acta*, v.  
226 67, p. 75–83.

227 Cuif, J.-P., Dauphin, Y., Farre, B., Nehrke, G., Nouet, J., and Salomé, M., 2008, Distribution of  
228 sulphated polysaccharides within calcareous biominerals suggests a widely shared two-step  
229 crystallization process for the microstructural growth units: *Mineralogical Magazine*, v. 72,  
230 p. 233–237.

231 Fernández-Díaz, L., Fernández-González, Á., and Prieto, M., 2010, The role of sulfate groups in  
232 controlling CaCO<sub>3</sub> polymorphism: *Geochimica et Cosmochimica Acta*, v. 74, p. 6064–  
233 6076.

234 Fike, D.A., Bradley, A.S., and Rose, C.V., 2015, Rethinking the Ancient Sulfur Cycle: *Annual*  
235 *Reviews of Earth and Planetary Sciences*, v. 43, p. 593–622.

236 Fike, D.A., and Grotzinger, J.P., 2008, A paired sulfate-pyrite  $\delta^{34}\text{S}$  approach to understanding  
237 the evolution of the Ediacaran-Cambrian sulfur cycle: *Geochimica et Cosmochimica Acta*,  
238 v. 72, p. 2636–2648.

239 Garrels, R.M., and Lerman, A., 1981, Phanerozoic cycles of sedimentary carbon and sulfur:  
240 *Proceedings of the National Academy of Sciences*, v. 78, p. 4652–4656.

241 Gill, B.C., Lyons, T.W., Young, S.A., Kump, L.R., Knoll, A.H., and Saltzman, M.R., 2011,  
242 Geochemical evidence for widespread euxinia in the Later Cambrian ocean: *Nature*, v. 469,  
243 p. 80–83.

244 Gorzelak, P., Stolarski, J., Mazur, M., and Meibom, A., 2013, Micro- to nanostructure and  
245 geochemistry of extant crinoidal echinoderm skeletons: *Geobiology*, v. 11, p. 29–43.

246 Jones, D.S., and Fike, D.A., 2013, Dynamic sulfur and carbon cycling through the end-  
 247 Ordovician extinction revealed by paired sulfate-pyrite  $\delta^{34}\text{S}$ : Earth and Planetary Science  
 248 Letters, v. 363, p. 144–155.

249 Jones, D.S., Fike, D.A., Finnegan, S., Fischer, W.W., Schrag, D.P., and McCay, D., 2011,  
 250 Terminal Ordovician carbon isotope stratigraphy and glacioeustatic sea-level change across  
 251 Anticosti Island (Québec, Canada): Geological Society Of America Bulletin, v. 123, p.  
 252 1645–1664.

253 Kaufman, A.J., Hayes, J.M., Knoll, A.H., and Germs, G.J.B., 1991, Isotopic compositions of  
 254 carbonates and organic carbon from upper Proterozoic successions in Namibia: stratigraphic  
 255 variation and the effects of diagenesis and metamorphism.: Precambrian Research, v. 49, p.  
 256 301–327.

257 Kump, L.R., Arthur, M.A., Patzkowsky, M.E., Gibbs, M.T., Pinkus, D.S., and Sheehan, P.M.,  
 258 1999, A weathering hypothesis for glaciation at high atmospheric  $\text{pCO}_2$  during the Late  
 259 Ordovician: Palaeogeography, Palaeoclimatology, Palaeoecology, v. 152, p. 173–187.

260 Present, T.M., Paris, G., Burke, A., Fischer, W.W., and Adkins, J.F., 2015, Large Carbonate  
 261 Associated Sulfate isotopic variability between brachiopods, micrite, and other sedimentary  
 262 components in Late Ordovician strata: Earth and Planetary Science Letters, v. 432, p. 187–  
 263 198.

264 Ries, J.B., Fike, D.A., Pratt, L.M., Lyons, T.W., and Grotzinger, J.P., 2009, Superheavy pyrite  
 265  $\delta^{34}\text{S}_{\text{pyr}} > \delta^{34}\text{S}_{\text{CAS}}$  in the terminal Proterozoic Nama Group, southern Namibia: A  
 266 consequence of low seawater sulfate at the dawn of animal life: Geology, v. 37, p. 743–746.

267 Rose, C.V., Fischer, W.W., Finnegan, S., and Fike, D.A., 2019, Records of carbon and sulfur  
 268 cycling during the Silurian Ireviken Event in Gotland, Sweden: Geochimica et  
 269 Cosmochimica Acta, v. 246, p. 299–316.

Saltzman, M.R., Runnegar, B., and Lohmann, K.C., 1998, Carbon isotope stratigraphy of upper Cambrian (Steptoean stage) sequences of the eastern Great Basin: Record of a global oceanographic event: *Bulletin of the Geological Society of America*, v. 110, p. 285–297.

Tamenori, Y., Yoshimura, T., Luan, N.T., Hasegawa, H., Suzuki, A., Kawahata, H., and Iwasaki, N., 2014, Identification of the chemical form of sulfur compounds in the Japanese pink coral (*Corallium elatius*) skeleton using  $\mu$ -XRF/XAS speciation mapping: *Journal of Structural Biology*, v. 186, p. 214–223.

Trong Nguyen, L., Rahman, M.A., Maki, T., Tamenori, Y., Yoshimura, T., Suzuki, A., Iwasaki, N., and Hasegawa, H., 2014, Distribution of trace element in Japanese red coral *Paracorallium japonicum* by  $\mu$ -XRF and sulfur speciation by XANES: Linkage between trace element distribution and growth ring formation: *Geochimica et Cosmochimica Acta*, v. 127, p. 1–9.

Wotte, T., Shields-Zhou, G., and Strauss, H., 2012, Carbonate-associated sulfate: Experimental comparisons of common extraction methods and recommendations toward a standard analytical protocol: *Chemical Geology*, v. 326–327, p. 132–144.

## FIGURE CAPTIONS

Figure 1: (A) X-ray Absorption Near-edge Structure measurements across the S K-edge resolve sulfate from sulfide and other S phases, as well as enable the identification of multiple forms of (inorganic and organic) sulfate. Spectra localities from a crinoidal grainstone (see GSA Data Repository). Inset: Spectra for S phases from [ESRF ID-21 Sulfur XANES Spectra Database](#). (B) Inorganic sulfate (2482.7 eV), distorted inorganic sulfate (2482.5 eV), and organosulfate (2481.4 eV) concentrations across a micritized rim of a non-skeletal grain (see Fig. 3D).

294

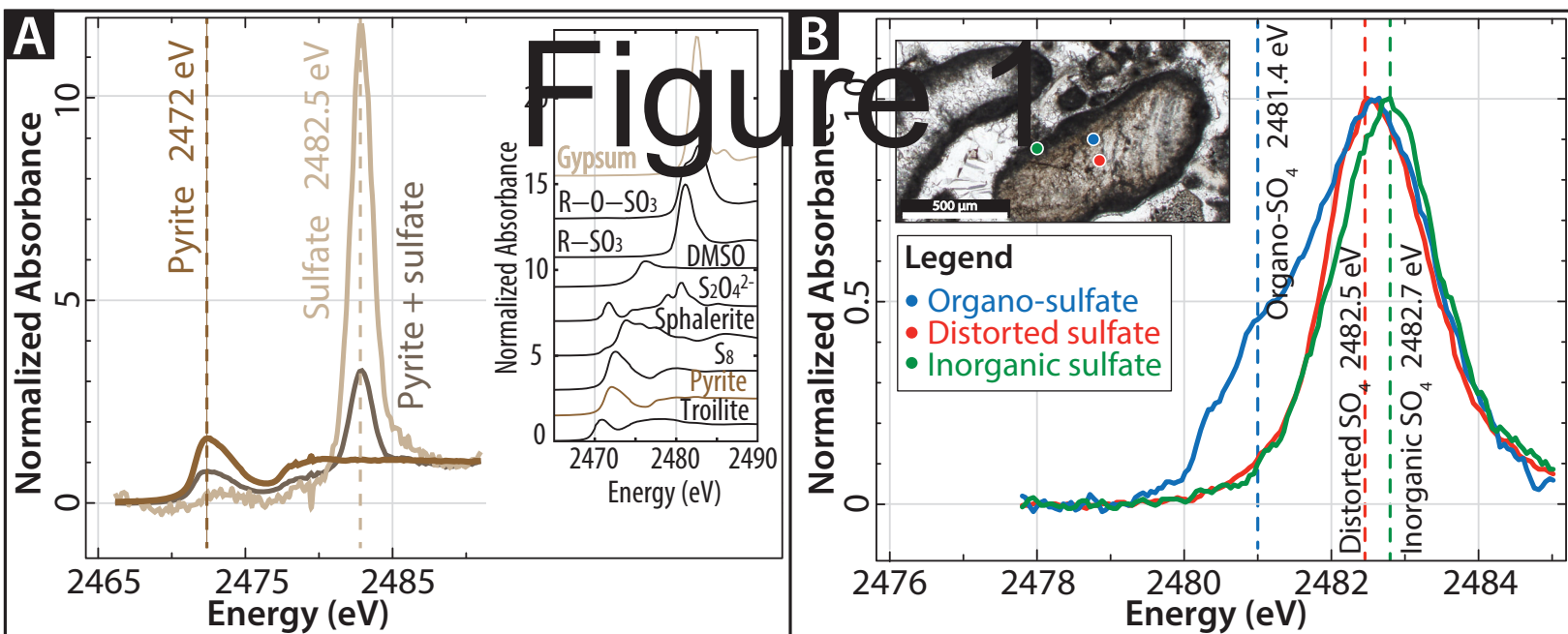
295 Figure 2: (A) Optical image through an oncoid grainstone featuring a replaced gastropod shell  
296 (right side of image). (B) Schematic diagram and associated legend of optical image highlighting  
297 different carbonate components with localities of spectral analyses. The data summary for the  
298 ROIs can be found at GSA Data Repository. (C) Corresponding sulfate abundances (2482.7 eV)  
299 showing the difference in the distribution of CAS within grains, between grains, and within the  
300 calcite cement. (D) Maps showing the abundance of inorganic sulfate, distorted sulfate, and  
301 organosulfate and a composite of the three moieties across micritized rim of grain (region  
302 outlined with red box in (A)). (E-F) Complementary elemental abundance maps (warm colors  
303 indicate increased abundance) for Fe (E) and Mn (F).

304

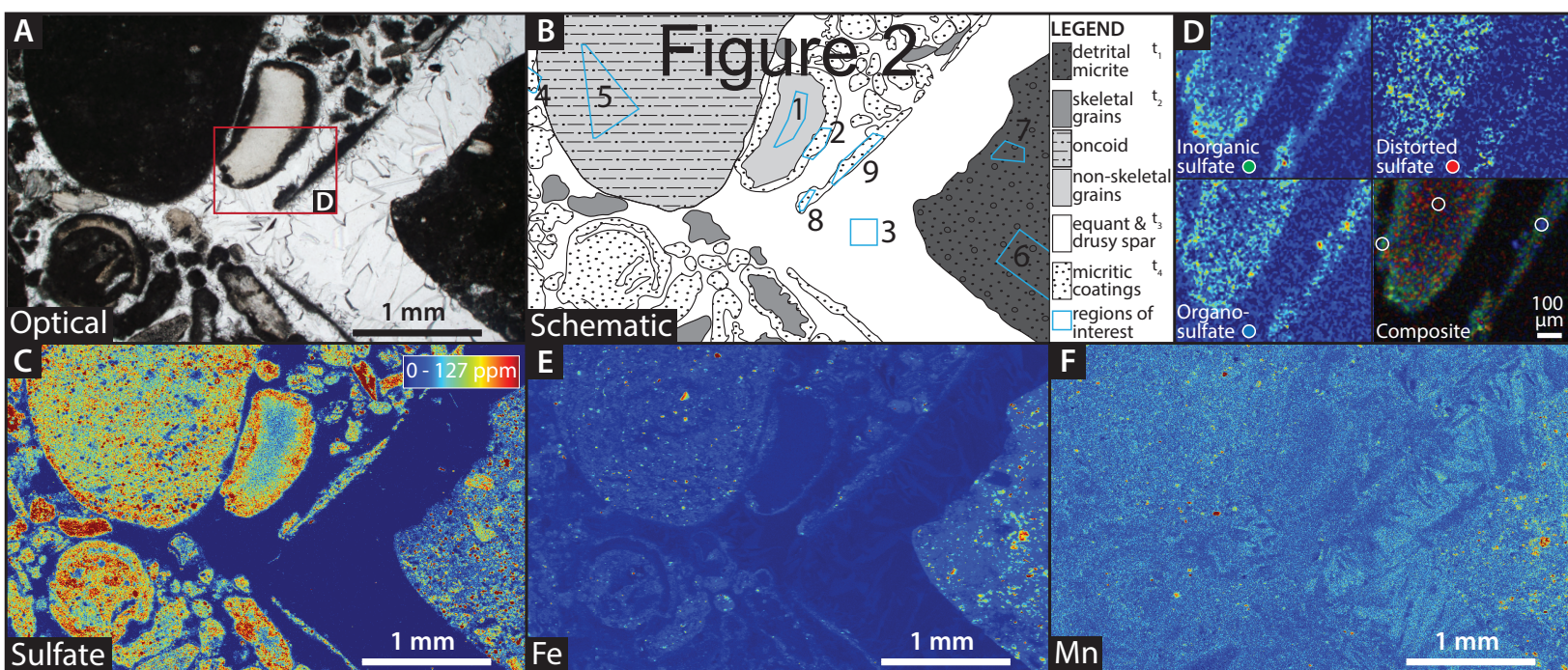
305 Figure 3: (A) Optical image through a gastropod shell. (B) Schematic diagram and legend of  
306 optical image highlighting different carbonate components with localities of spectral analyses.  
307 The data summary for the ROIs can be found at GSA Data Repository. (C) Corresponding  
308 sulfate abundances (2482.7 eV). (D) Maps showing the abundance of inorganic sulfate, distorted  
309 sulfate, organosulfate, and a composite of these moieties across a non-skeletal grain with a  
310 micritic coating (region outlined with red box in (A)). (E-F) Complementary elemental  
311 abundance maps (warm colors indicate increased abundance) for Fe (E) and Si (F).

312

313 Figure 4: Notched boxplots for sulfate concentrations in ROIs 1-9 (Fig. 2) and ROIs 10-19 (Fig.  
314 3). Each column represents the data from a ROI. The box encloses 50% of the data (25<sup>th</sup> to 75<sup>th</sup>  
315 percentile) and the whiskers extend 1.5\*interquartile range beyond the box. Points represent  
316 outliers as defined by Tukey's method. The width of the notch defines the 95% confidence  
317 interval of the median.









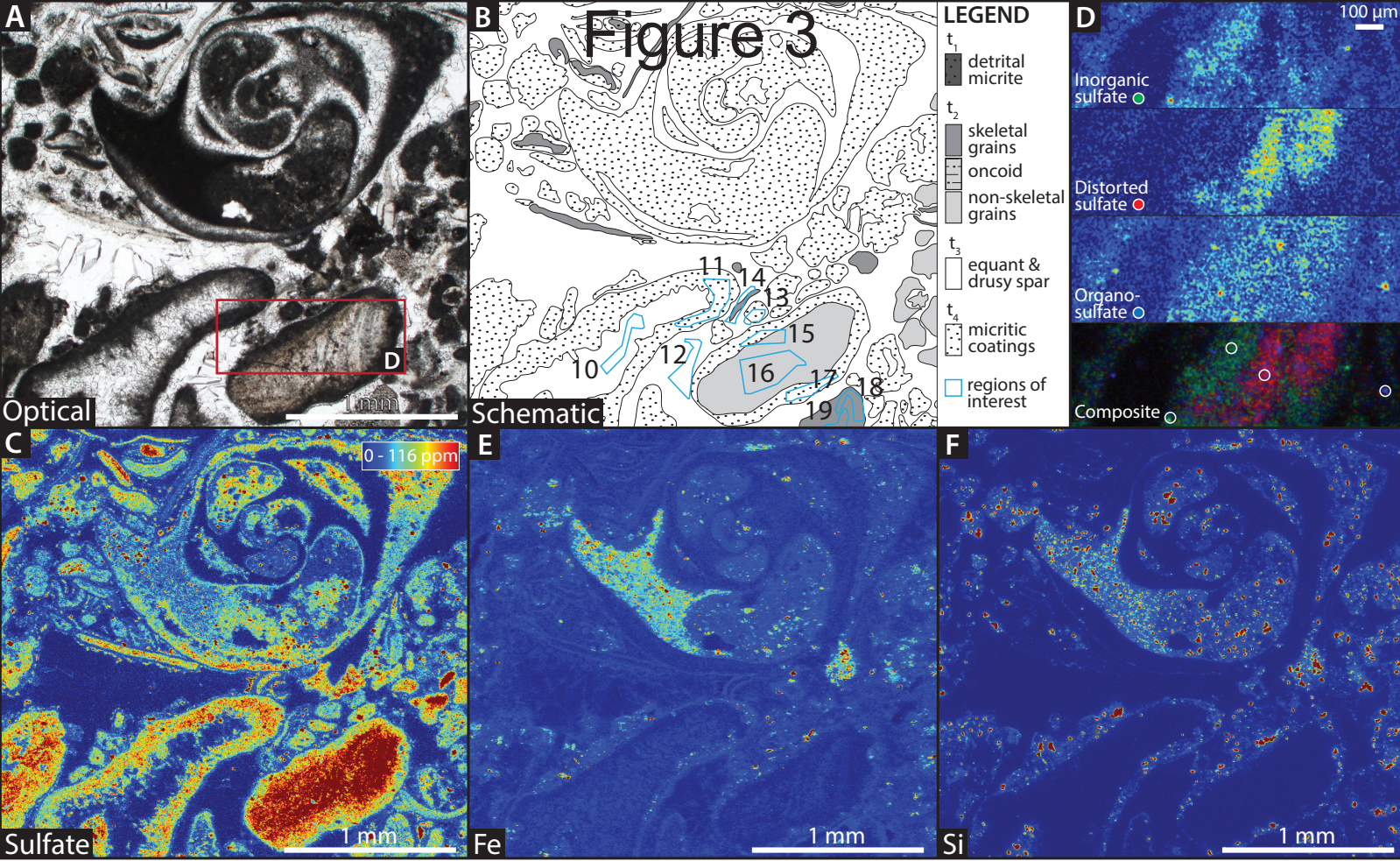


# Figure 4

